*Bangladesh Journal of Physics, Vol. **31**, Issue 1, pp. 1–16, June 2024*

INVITED PAPER

ENHANCEMENTS OF OPTOELECTRONIC PROPERTIES OF DOPED $CsSnCl_3$ FOR NEXT-GENERATION DEVICES

A. K. M. AKTHER HOSSAIN AND DHOLON KUMAR PAUL

Department of Physics, Bangladesh University of Engineering and Technology, Dhaka 1000, Bangladesh

**Corresponding author e-mail: akmhossain@phy.buet.ac.bd*

Received on 01.03.2024, Accepted for publication on 10.04.2024

DOI: *https://doi.org/10.3329/bjphy.v31i1.79516*

ABSTRACT

In advanced electrical and photovoltaic applications, inorganic metal halide perovskite materials have become strong contenders because of their remarkable properties. However, the pure form of cesium tin chloride exhibits suboptimal electro-optical capabilities, hindering its potential for achieving ideal optoelectronic efficiency. This study employs density functional theory to compute and analyze the structural, elastic, electrical, and optical properties of both pure $CsSnCl_3$ and its doped variants with *Ti*, *V*, *Cr*, *Mn*, *Sb*, *In*, *Fe*, *Cu*, and *Zn* at various concentrations. By maintaining consistent computational parameters, we explored the electrical and optical attributes of these materials and their respective ground states, aiming to identify the most promising doped phase of $CsSnCl_3$ for high-performance optoelectronic applications. Our findings not only highlight the potential of doped perovskite materials but also provide valuable insights for researchers and industry professionals in selecting the optimal doped phase of $CsSnCl_3$, paving the way for significant advancements in optoelectronics.

Keywords: *Metal halide perovskite, Structural properties, Optoelectronic properties*

1. INTRODUCTION

Metal-halide perovskites (MHPs) have captivated scientists worldwide due to their remarkable properties and immense potential for diverse applications, including photovoltaics, optoelectronics, and photocatalysis [1–4]. These materials exhibit a range of desirable characteristics, such as significant visible light absorption, tunable bandgap, low reflectivity, excellent charge-carrier mobility, high ductility, low recombination rates, and robust photoluminescence quantum yields [5]. These attributes have led to the widespread use of MHPs in electronic devices like photodetectors, LEDs, photovoltaics, and solar-to-fuel energy conversion systems. Despite significant advancements in perovskite solar cells since their inception, their photovoltaic efficiency still falls short of the single-gap Shockley-Queisser limit [6]. For instance, single-junction solar cells with a 1.34 eV bandgap have the potential to reach a 33% conversion efficiency, surpassing the theoretical maximum efficiency of 25-27% predicted by the Shockley-Queisser model [6]. As a result, extensive research has been dedicated to exploring the potential and enhancing the efficiency of perovskite solar cells [2,4,7,8]. Amid concerns regarding the high toxicity and environmental impact of lead-based compounds, there has been a concerted effort to find suitable substitutes for lead in perovskite materials [9]. Cesium tin chloride ($CsSnCl_3$), has emerged as a particularly promising candidate due to its abundance of raw materials and high stability [4,10–12]. However, the relatively large bandgap of $CsSnCl_3$ limits its optoelectronic performance. To overcome this limitation, various

doping techniques have been investigated to tune the bandgap and improve the optoelectronic properties of $CsSnCl_3$ [4].

Among these strategies, introducing the intermediate band (IB) or in-gap band (IGB) concept shows remarkable potential for enabling sub-bandgap absorption [13,14]. Materials with an IGB have a narrow band partially filled between the host semiconductor's valence and conduction bands (VB and CB, respectively) [15]. The IGB's generation of more electron-hole pairs may increase photocurrent, potentially increasing the efficiency of solar cells. A theoretical efficiency of up to 63.1% has been projected for cells using this method [15].

We explored the effects of doping $CsSnCl_3$ in the Sn site with six *d*-block elements, *Ti*, *V*, *Cr*, *Mn*, *Zn*, *Cu*, and *Fe*, and two *p*-block elements, *Sb* and *In*. We doped them at different concentrations (12.5% and 25%) to determine the ideal doping phases. Electronic properties have been examined all across the phases to establish the causative factors of their optical and electrical properties.

2. COMPUTATIONAL METHOD

The Cambridge Serial Total Energy Package (CASTEP) [16–18] code was employed to conduct first-principles calculations based on density functional theory (DFT) [17]. To predict the exchange-correlation energy, the Perdew-Burke-Ernzerhof (PBE) [19] functional within the generalized gradient approximation (GGA) framework was utilized. The geometry of the $CsSnCl_3$ crystal structure was optimized using the Broyden-Fletcher-Goldfarb-Shanno (BFGS) minimization method [20]. For special k-point sampling of the Brillouin zone (BZ), the Monkhorst-Pack scheme was applied [21]. For a pure single cell, a plane wave energy cutoff of 600 eV and a k-point grid of 14×14×14 was used. In contrast, for doped structures, a reduced energy cutoff of 350 eV and a 3×3×3 k-point grid were selected. Convergence criteria were set with an energy tolerance of 2.0×10^{-5} eV/atom, a maximum force on atoms of 0.05 eV/Å, a maximum stress of 0.10 GPa, and a maximum atomic displacement of 2.0×10^{-3} Å to optimize the structures while analyzing their structural, optical, and electronic properties. To reconcile the theoretical and observed bandgap values of pure and doped $CsSnCl_3$, its optical properties were calculated using a scissor value of 1.844 eV. The objective was to bring the theoretical bandgap value of 0.956 eV closer to the experimental value of 2.8 eV. This underestimating of the theoretical bandgap value is a known shortcoming of the DFT calculation method, which does not account for the discontinuity in the exchange correlation potential. The scissor operator, which creates a rigid shift of the unoccupied conduction band, was utilized to close the gap between the theoretical and actual results.

3. STRUCTURAL PROPERTIES

The lead-free perovskite $CsSnCl_3$ features a cubic structure, identified by the space group $Pm\bar{3}m$ (No. 221) [22]. The atomic configuration is as follows: *Cs* atoms are located at the corners (0, 0, 0), Sn atoms are at the body center (0.5, 0.5, 0.5), and *Cl* atoms are positioned at the face centers (0, 0.5, 0.5) [22], respectively. Fig. 1 illustrates the unit cell of $CsSnCl_3$, composed of corner-sharing [$SnCl_6$] octahedra, with *Cs* cations occupying a 12-fold coordination site at the center of a cube formed by eight octahedra [23].

To introduce doping in $CsSnCl_3$, we used the supercell method. The unit cell of $CsSnCl_3$ consists of 1 *Cs* atom, 1 *Sn* atom, and 3 *Cl* atoms, totaling 5 atoms. By constructing a 2×2×2 supercell, the number of atoms increases to 40: 8 *Cs*, 8 *Sn*, and 24 *Cl*. We then replaced *Sn* atoms at the *B* site in the ABX_3 structure of the $CsSnCl_3$ supercell with dopant atoms at various concentrations. For a 12.5% doping concentration, the formula is $CsSn_{1-0.125}X_{0.125}Cl_3$, and for a 25% doping concentration, it is $CsSn_{1-0.25}X_{0.25}Cl_3$, where *X* represents *Ti*, *V*, *Cr*, *Mn*, *Fe*, *Cu*, *Zn*, *Sb*, or *In*.

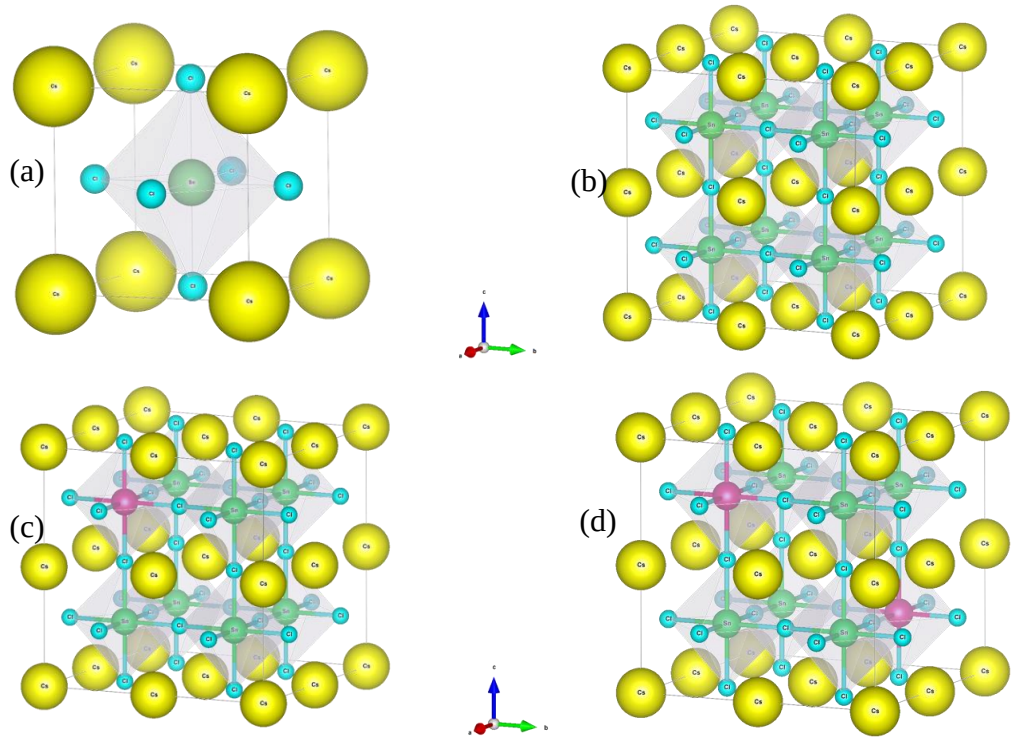

Fig. 1. Structural Representation of *$CsSnCl_3$*: (a) Pure crystal cell, (b) Assembled 2×2×2 pristine supercell, (c) 12.5% doping at the *Sn* site (shown in magenta), (d) 25% doping across two *Sn* sites.

Table 1 displays the calculated lattice parameters and unit cell values for pure and doped *$CsSnCl_3$* samples. The values align well with previous experimental [24] and theoretical [22] studies. The calculations reveal a reduction in lattice constants and volume for the doped samples, likely due to the smaller ionic radius of the dopant elements compared to the Sn^{2+} ion.[25]

4. OPTICAL PROPERTIES

We analyzed the optical characteristics of the studied phases, focusing on the absorption coefficient, real and imaginary parts of the dielectric function, reflectivity, and photoconductivity. These properties were evaluated up to a photon energy of 27 eV to gain insight into the materials' behavior under solar and high-energy radiation. As we present 9 doping elements across 16 total phases, we have segregated them into two groups for more straightforward analysis and comparison. The phases with the desired characteristics are grouped and separated from the other phases.

The absorption coefficient is crucial in designing and improving optoelectronic devices, including photodetectors and solar cells. Modifying the absorption coefficient and bandgap energy allows for optimizing a material's performance for targeted applications. For instance, solar cells need a high absorption coefficient in the visible spectrum to capture the maximum amount of light and generate a significant photocurrent. The absorption coefficient is directly influenced by the bandgap energy.[22] When incident photon energies are less than the bandgap energy, the absorption coefficient is often low, and the material is transparent to incident light. The absorption coefficient rapidly increases when the photon energy approaches or exceeds the bandgap energy, and the material becomes opaque.

Table 1. Comparative analysis of unit cell volumes and lattice parameters for undoped and doped $CsSnCl_3$.

Phase	*a* (Å)			V (Å^3)
	This work	Other works	Experimental	
$CsSnCl_3$	5.559	5.617, 5.620 [26], 5.610 [27]	5.560 [28], 5.573 [24]	171.78
$CsSn_{1-0.125}Ti_{0.125}Cl_3$	5.575	-	-	173.018
$CsSn_{1-0.25}Ti_{0.25}Cl_3$	5.496	5.531	-	166.012
$CsSn_{1-0.125}V_{0.125}Cl_3$	5.521	5.559	-	168.288
$CsSn_{1-0.25}V_{0.25}Cl_3$	5.441	5.481	-	161.077
$CsSn_{1-0.25}Cr_{0.25}Cl_3$	5.439	5.463	-	160.90
$CsSn_{1-0.125}Mn_{0.125}Cl_3$	5.511	5.541, 5.54 [26]	-	167.37
$CsSn_{1-0.25}Mn_{0.25}Cl_3$	5.437	5.461	-	160.72
$CsSn_{1-0.25}Fe_{0.25}Cl_3$	5.441	-	-	161.077
$CsSn_{1-0.125}Cu_{0.125}Cl_3$	5.522	-	-	168.379
$CsSn_{1-0.25}Cu_{0.25}Cl_3$	5.456	-	-	162.413
$CsSn_{1-0.125}Zn_{0.125}Cl_3$	5.568	-	-	172.622
$CsSn_{1-0.25}Zn_{0.25}Cl_3$	5.496	-	-	166.012
$CsSn_{1-0.125}In_{0.125}Cl_3$	5.605	-	-	176.086
$CsSn_{1-0.25}In_{0.25}Cl_3$	5.581	-	-	173.834
$CsSn_{1-0.125}Sb_{0.125}Cl_3$	5.605	-	-	176.086
$CsSn_{1-0.25}Sb_{0.25}Cl_3$	5.599	-	-	175.521

We split all of the doped materials we tested into two groups based on their absorption in the visible (300 – 800 nm) part of the spectrum: those with exceptional absorption and those with little to no absorption in that region. From Figs. 2 (a) and (c), we can see that (*Cr* at 25%, *Ti* at 25%, *V* at 12.5% and 25%, and *Mn* at 12.5% and 25%) doped $CsSnCl_3$ phases showed an impressive absorption coefficient all over the spectrum. *V* exhibits the maximum peak in the visible spectrum at a concentration of 12.5%, and the characteristic is as follows: *V* 12.5 % > *V* 25 % > *Ti* 25 % > *Mn* 25 % > *Cr* 25 % > *Mn* 12.5 % phase, unlike the pure $CsSnCl_3$, which exhibited no apparent peak. In Figs. 2 (b) and (d), the *AM1.5G* solar spectrum is used as a reference in the background, commonly employed by researchers and manufacturers to assess solar devices' performance under realistic conditions. This standard spectrum enables more precise comparisons and evaluations across various locations and applications. Figs. 2. (b) and (d) demonstrate the absorption coefficient of other phases of doped materials that showed little to no peaks in the whole spectrum.

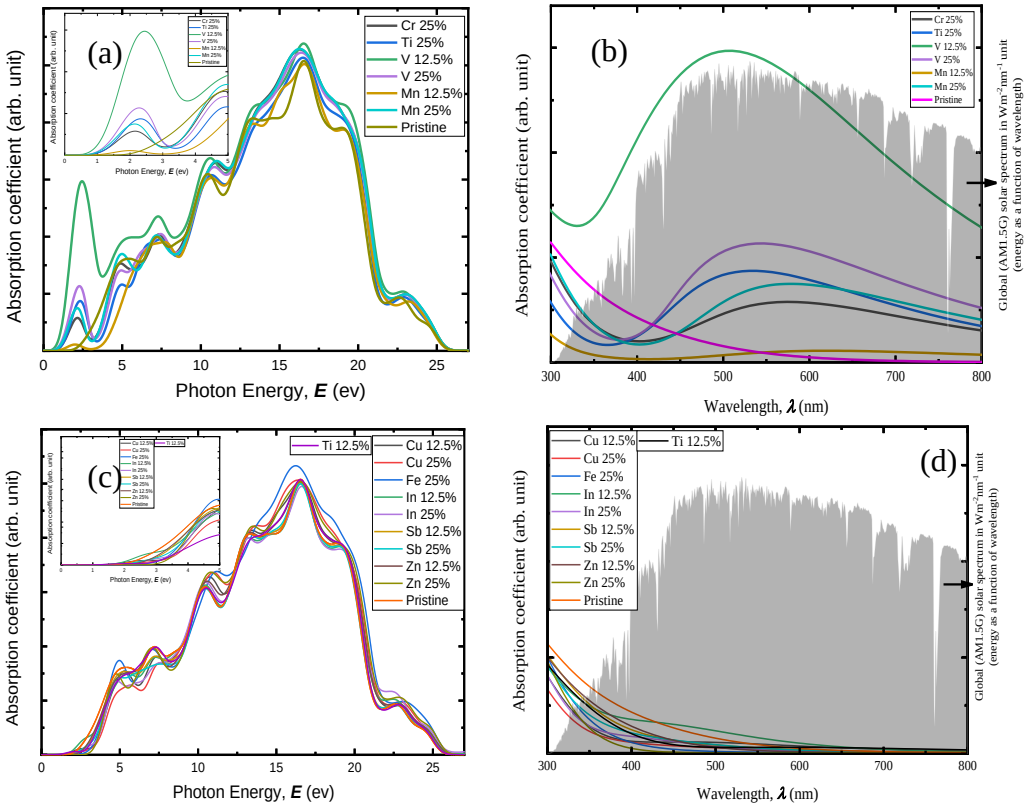

Fig. 2. Computed optical absorption spectra for doped *CsSnCl3* relative to incident photon energies. (a), (b) doped with *Cr* 25%, *Ti* 25%, *V* 12.5% & 25%, *Mn* 12.5% & 25% concentration. (c), (d) doped with *Cu* 12.5% & 25%, *Fe* 25%, *In* 12.5% & 25%, *Sb* 12.5% & 25%, *Zn* 12.5% & 25% concentration.

Understanding the interaction between a material and incident photons requires analyzing the real and imaginary components of the dielectric function. The performance of optoelectronic devices can be significantly enhanced by increasing the real part of the dielectric function. For instance, in solar cells, a higher real part enhances light absorption and increases power output, enabling the active layer to capture more light. Likewise, in photodetectors, a higher real component boosts sensitivity to incoming light, leading to better signal-to-noise ratio and overall device performance. The imaginary part provides insights into the electronic structure and light absorption response of the material. This information is crucial for developing efficient devices, as a high imaginary component indicates effective light absorption within a certain photon energy range, which is beneficial for both solar cells and photodetectors. Figs. 3 (a) and (b) show that the real and imaginary parts of the dielectric function both peak in the low-energy (Visible) region. Both 12.5 and 25% concentrations of V doping showed the highest peak where the trend is as follows: *V* 12.5% > *V* 25% > *Mn* 25% > *Ti* 25% > *Cr* 25% > *Mn* 12.5% > Pristine.

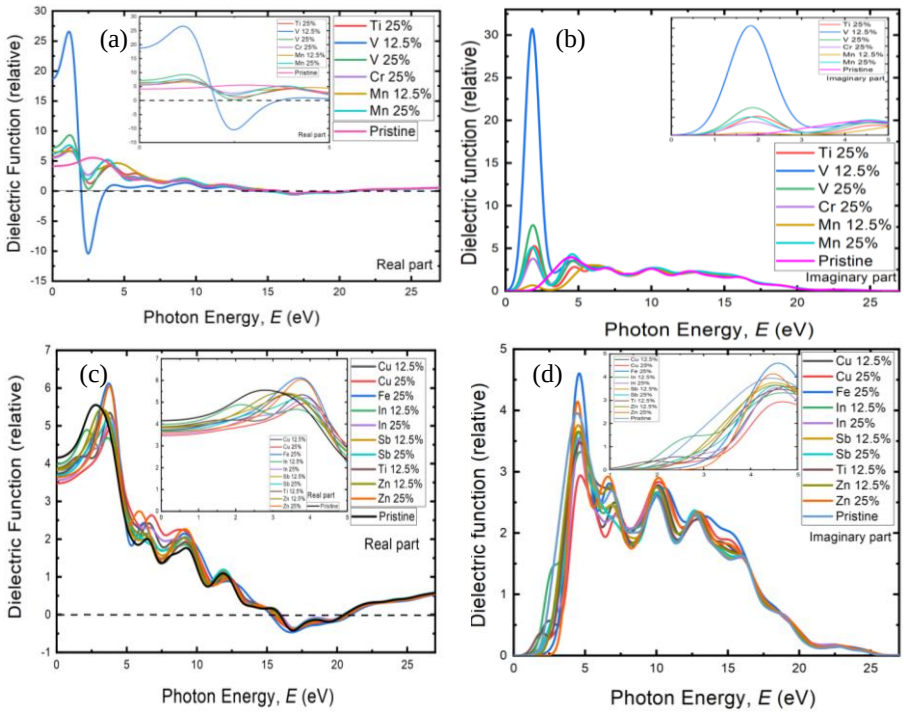

Fig. 3. Real (a), (c) and Imaginary (b), (d) components of the dielectric function based on computational data.

Similarly, Figs. 3.(c), (d) show real and imaginary parts of the dielectric function of *Cu* 12.5%, Cu 25%, *Fe* 25%, *In* 12.5%, *In* 25%, *Sb* 12.5%, *Sb* 25%, *Ti* 12.5% *Zn* 12.5% and *Zn* 25%, respectively. Here, hardly any peaks in regions of visible energy have been recorded. This indicates that these doped phases of $CsSnCl_3$ are less likely to interact with visible-range photons. A low real component of the dielectric function implies a low index of refraction, which means that light traveling through the material will not be significantly twisted or slowed down. This can affect the material's capacity to absorb light, resulting in diminished device performance in applications such as solar cells and photodetectors. A low imaginary component of the dielectric function suggests that the material has few electronic transitions and is light transparent.

Complex conductivity, including real and imaginary parts, quantifies how effectively a material can conduct electricity when exposed to an electromagnetic field. The real component indicates how well the material can transport electricity when exposed to an external electric field. It calculates the efficiency with which charges can pass through a substance when no magnetic field is present. If the real component of a substance's conductivity has a high value, it is regarded as a good conductor. If this number is low, however, the substance is either an insulator or a poor conductor. The imaginary part of the conductivity (Fig. 4b and d) shows a material's ability to hold an electrical charge in an electric field. It evaluates the material's magnetic field-induced charge displacement responsiveness. A material is either a poor dielectric or a conductor if its imaginary conductivity component is low.

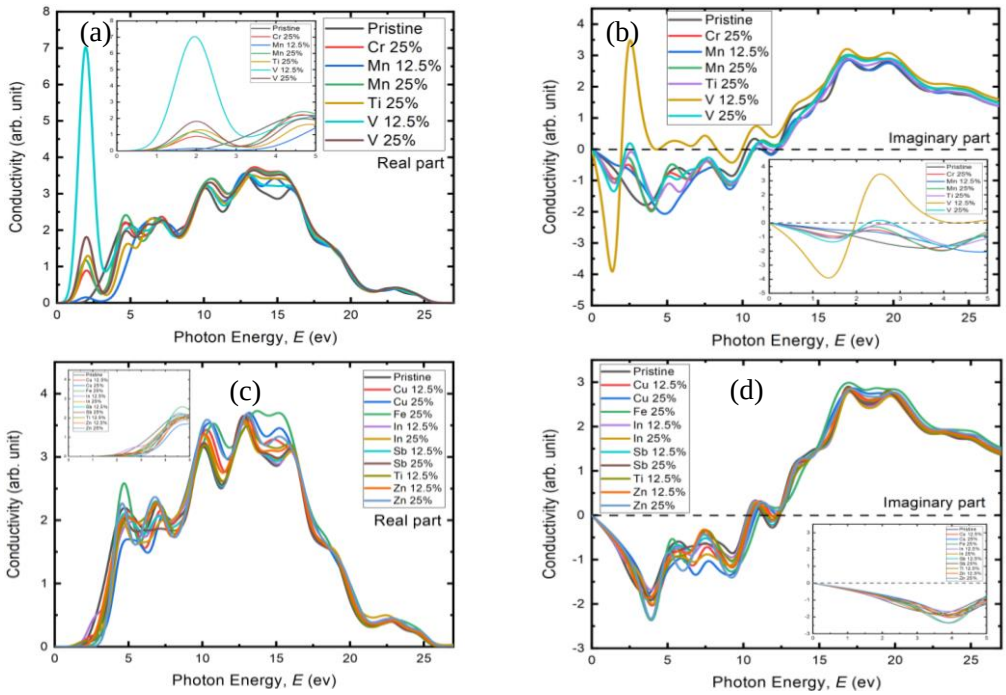

Fig. 4. Computed conductivity spectra: (a), (c) real part and (b), (d) imaginary part.

The *Cr* 25%, *Ti* 25%, *V* 12.5% & 25%, and *Mn* 12.5% & 25% doped concentrations consistently display a sharp peak in the visible energy region of the real part of conductivity, as seen in Figs. 4(a) and 4(c), maintaining the same pattern observed previously. That is essential for optoelectronics applications. For all doped phases, the imaginary component of complex conductivity has a low value in the low-energy region, which indicates that they are excellent conductors in that energy range. A sharp peak of *V* 12.5% indicates that the material is suitable for use as a dielectric in the peak energy region.

Reflectivity measures how well a material reflects incoming light energy from its surface, which is crucial for evaluating its potential in photovoltaic applications. The *V* 12.5% doped phase shows maximum reflectivity at 3 eV photon energy, with a steep decline as photon energy increases, as indicated by the calculated reflectivity spectra. in Fig. 5(a). Compared to pure $CsSnCl_3$, all doped phases except for *V* 12.5% exhibit low reflectivity from the 300-470 nm wavelength region. The reason behind this is discussed in the section on electronic properties.

The high reflectivity of the *V* 12.5% sample in the visible wavelength region makes it less efficient for use in solar cell applications. Further studies should aim to lower the high reflectivity across the visible region, which could significantly enhance light absorption and, as a result, improve the performance of solar cells. Compared to pure $CsSnCl_3$, Fig. 5(c) reveals no significant deviations for any of the doped phases across the entire spectrum.

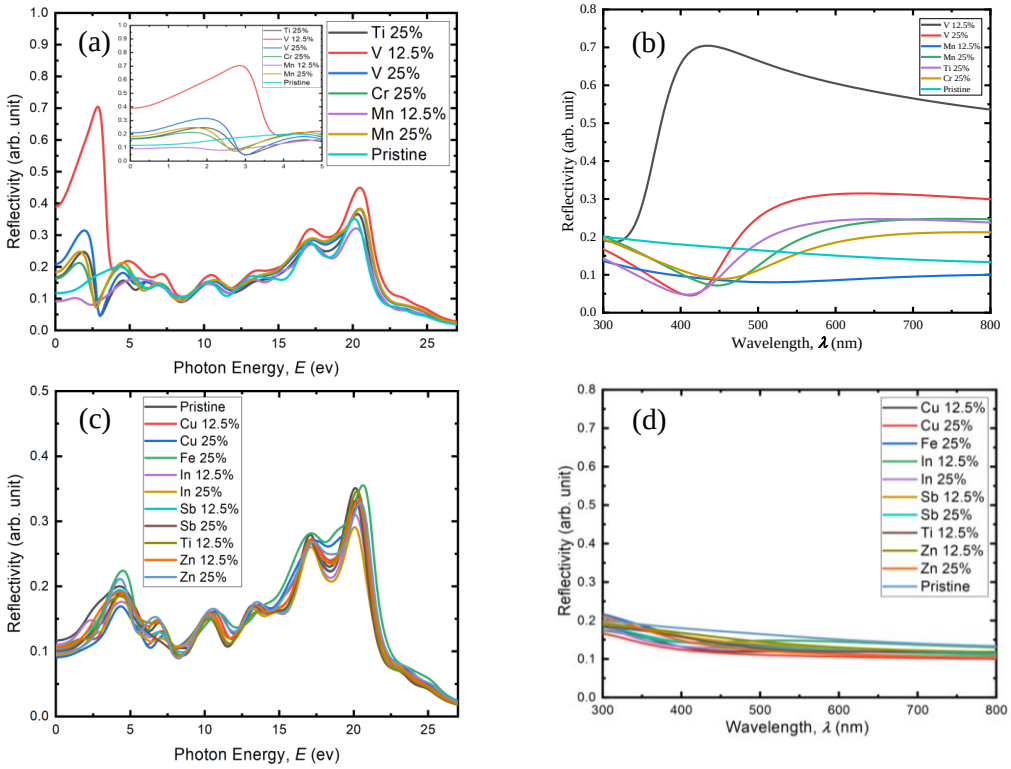

Fig. 5. Computed spectra of reflectivity.

5. ELECTRONIC PROPERTIES

As evidenced by their optical properties, some of the examined phases exhibited more remarkable optical phenomena than others. The electronic properties of all these phases have been analyzed to investigate the potential cause of optical phenomena further.

The anticipated band structure and density of states for both pure and doped materials are illustrated in Figs. 6 and 7, respectively. In semiconductor theory, the bands closest to the Fermi level are essential for understanding a material's true properties. Therefore, the focus is on the band contributions near the Fermi level. The bandgap characteristics depend on the lowest point of the conduction band (CB) and the highest point of the valance band (VB). Fig. 6(g) shows that in pristine $CsSnCl_3$, the CB minimum and VB maximum align at the same k-point, confirming a direct bandgap. Our calculations estimate the direct bandgap of pure $CsSnCl_3$ to be 0.956 eV, aligning with the theoretical values in the existing literature [11,26,29,30]. Precision of this study is further supported by the fact that the density of states (DOS) of $CsSnCl_3$ shown in Fig. 7 (q) is a perfect match with the study that was previously published [11,26,29,30].

The GGA method underestimates the bandgap, producing a value lower than the experimentally measured 2.8 eV [31]. This underestimation is a known limitation of the GGA method due to its

approximation of electron-electron exchange and correlation effects. The local density approximation (LDA) and LDA+ Hubbard parameter (U) methods also share this limitation. Although hybrid functionals [32] have been developed to address this issue, they come with their own challenges. The GGA+U method [4,33], provides a partial solution to bridging the gap between experimental and theoretical bandgap values, but this process is computationally very demanding.

Even though the bandgap is typically underestimated using the GGA approach, this comparative investigation of the band structure and DOS of pure and metal-doped $CsSnCl_3$ samples is insensitive to these limitations [26]. As it is seen in optical properties, doped phases that showed maximum visible range photon absorbance are *V* 12.5% > *V* 25% > *Ti* 25% > *Mn* 25% > *Cr* 25% > *Mn* 12.5%.

From Figs. 6(a) *Cr* 25%, (b) *Ti* 25%, (c) *Mn* 12.5%, (d) *V* 12.5%, (e) *V* 25%, (f) *Mn* 25%, all of them show the creation of intermediate stated in between the CBM and VBM. Here, intermediate states in the bandgap diagram refer to energy levels that exist within the bandgap of a material due to doping.

Analyzing the band structures of *Mn* 12.5% and 25% doped $CsSnCl_3$ in Figs. 6(c) and (f), we observed that the CB minimum and VB maximum are at different k-points for both, indicating an indirect bandgap. Our findings show that *Mn* 12.5% doped $CsSnCl_3$ has an indirect bandgap of 0.669 eV, which closely aligns with reported values, confirming the accuracy of this study. The 25% *Mn*-doped phase has an indirect bandgap of 1.439 eV, due to the VBM shifting to a lower energy region. On both occasions, a very thin intermediate state is observed from DOS, which reveals that the Mn-3d orbital causes this state. For *Mn* 12.5%, the width of the intermediate band (IB) to the CBM is 0.353 eV, and the IB to the VBM is 0.316 eV. For *Mn* 25%, the calculations are 0.354 eV in IB to CBM and 0.354 eV in IB to VBM.

Figs. 6(d) and (e) illustrate the band structures for the *V* 12.5% and *V* 25% doped phases, respectively. In the *V* 12.5% doped phase, both the CB minimum and VB maximum are located at the gamma (G) sites, while in the *V* 25% phase, the CB minimum is at the Q point, and the VB maximum at the G point. Our calculations indicate that *V* 12.5% has a direct bandgap of 1.106 eV, whereas *V* 25% exhibits an indirect bandgap of 2.749 eV. As the doping concentration increases, so does the bandgap, with the *V* 25% phase showing a more profound shift in CBM than the *V* 12% phase. Here, for V 12.5%, the IB is located below the CBM as an overlapped condition with the conduction band, and the IB in the *V* 25% phase is located at 0.549 eV below CBM. IB is above 1.782 eV of VBM in the *V* 25% phase.

Figs. 6(b) and (h) exhibit the band diagrams of *Ti* at a concentration of 12.5% and 25%, respectively. CB minimum and VB maximum occur at gamma (Q) and (G) sites, respectively, according to the electronic band structure of the 12.5% doped *Ti* phase. For *Ti* 25% dope, the CB minimum is at Q, and the VB maximum is at G. According to our calculations, *Ti* 12.5% doped phase has an indirect bandgap of 1.244 eV, while *V* 25% phase has an indirect bandgap of 2.709eV. As the doping concentration increased, the band gap widened. Compared to the *Ti* 12% doped phase, the CBM of the *Ti* 25% doped phase has shifted more profoundly into the low energy region, as indicated by the band structure. Here, for *Ti* 12.5%, the IB is positioned below the CBM due to overlap with the conduction band, whereas for *Ti* 25%, the IB is positioned at 0.392 eV below the CBM. IB exceeds 1.956 eV from VBM in the 25% doped phase of *Ti*.

Fig. 6(a) illustrates the band structure of the *Cr* 25% phase of $CsCnCl_3$. The CBM is positioned between the G and F points, whereas the VBM is positioned at the G points, indicating an indirect bandgap of 2.381eV. Near the Fermi level, 0.591 eV below CBM and 1.506 eV above VBM, a broad intermediate band is identified.

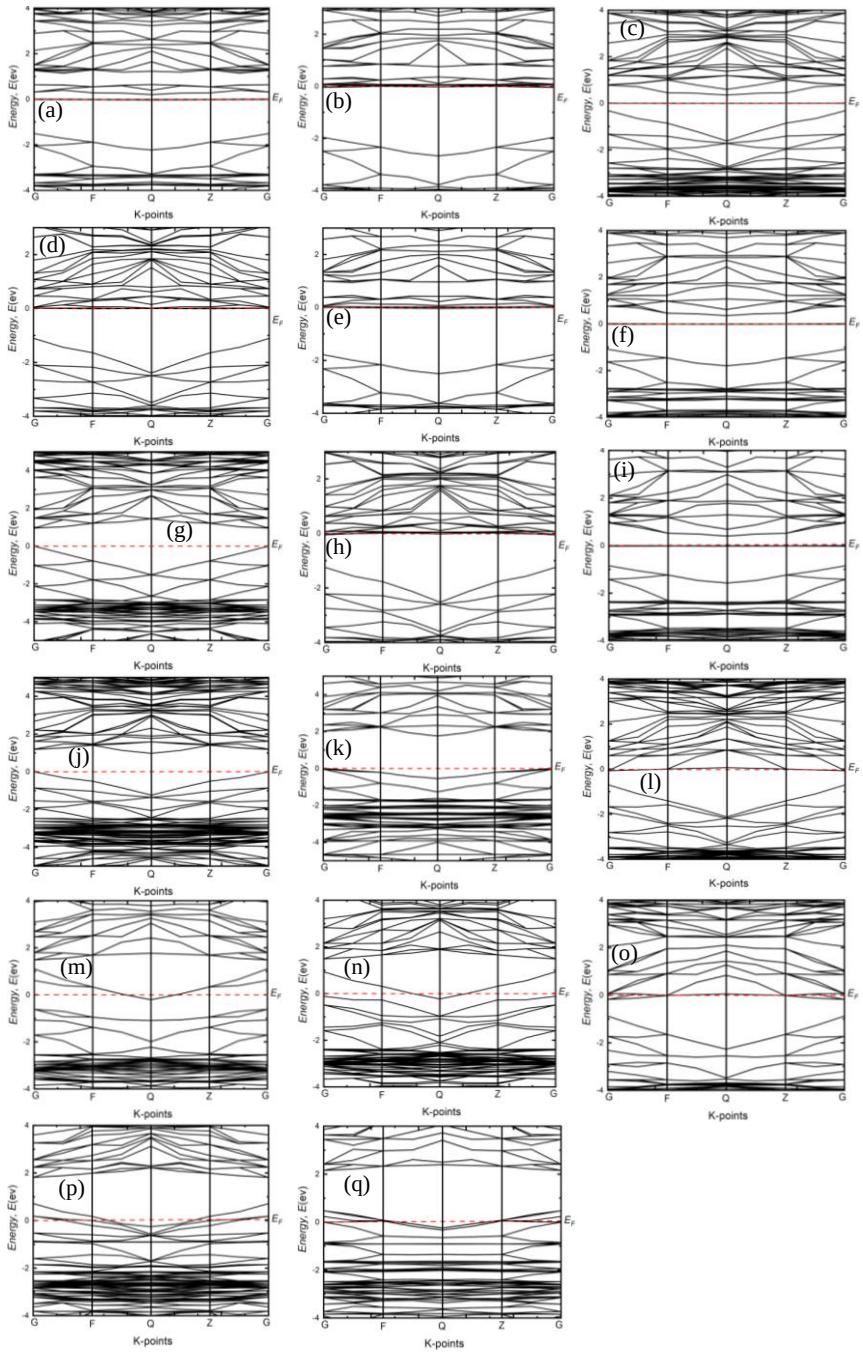

Fig. 6. The band structure of (a) *Cr* 25%, (b) *Ti* 25%, (c) *Mn* 12.5%, (d) *V* 12.5%, (e) *V* 25%, (f) *Mn* 25%, (h) *Ti* 12.5%, (i) *Fe* 25%, (j) *Zn* 12.5%, (k) *Zn* 25%, (l) *Sb* 12.5%, (m) *In* 12.5%, (n) *In* 25%, (o) *Sb* 25%, (p) *Cu* 12.5% and, (q) *Cu* 25% doped phases along with, (g) pristine $CsSnCl_3$ perovskites.

From Fig. 6(i), the band structure diagram of Fe 25% doped phase, the CB minimum is at the Q point, and the VB maximum is at the G- point. Our analysis indicated that the 25% Fe doped phase has an indirect bandgap of 1.247 eV. At zero Fermi level, a narrow IB is observed; the IB is located 0.398eV below the CBM and 0.848eV above the VBM.

Figs. 6 (j) and (k) exhibit the band diagrams of *Zn* at doping levels of 12.5% and 25%, respectively. On analyzing the band structures of *Zn* 12.5% and 25% doped $CsSnCl_3$, we discovered that the minimum of the CB and the maximum of the VB are at distinct k-points, indicating an indirect bandgap. The indirect bandgap of $CsSnCl_3$ doped with 12.5% *Zn* and 25% *Zn* is found to be 0.979 and 1.756% eV, respectively.

There has been no observation of an intermediary band between the bandgaps of both phases. Figs. 6 (p) and (q) represent the band structure diagrams of Cu at concentrations of 12.5% and 25%, respectively. CB minimum and VB maximum occur at the same gamma (G) values during both doping phases. According to the electronic band structure of the 12.5% and 25% doped Cu phases, they are direct bandgap materials with respective bandgap values of 1.1 and 1.684 eV.

The band structure of the *Sb* 12.5% diluted and *Sb* 25% diluted phases are shown in Figure 6 (l) and (o), respectively. Both the CB minimum and the VB maximum in the *Sb* 12.5% and *Sb* 25% doped phases occur at the same gamma (G) sites, indicating a direct bandgap material, as shown by their respective electronic band structures. We find that the direct bandgap of *Sb* at 12.5% is 0.63 eV, while that of *Sb* at 25% is 0.703 eV.

Figs. 6(m) and (n) show the band structure of *In* 12.5% and *In* 25% diluted phases, respectively. The CB minimum and VB maximum are both located at gamma (G) sites in the electronic band structure *In* 12.5% and *In* 25% doped phases. Based on our findings, 12.5% In the doped phase has a direct bandgap of 1.602 eV, whereas 25% has a direct bandgap of 2.099 eV.

The total density of states (TDOS) and partial density of states (PDOS) for all phases under study are presented in Fig. 7. These measurements offer insights into the material's electronic structure, including the shape and position of the valence and conduction bands. Doping introduces impurities into the semiconductor, significantly altering its electrical properties by creating additional energy levels within the bandgap, which are reflected in the TDOS. By analyzing the PDOS of doped materials, we can pinpoint the location and structure of these additional energy levels, helping to predict the material's response to light and the impact of specific doping concentrations on photoconductivity and other optoelectronic properties.

Fig. 7(q) illustrates that the VB of pure $CsSnCl_3$ is dominated by *Cl-3p* orbitals, with minor contributions from *Cs-6s*, *5p* and *Sn-5s, 5p*. CB represents a mixture of *Sn-5p*, *Cs-6s*, and *Cs-5p* orbitals. *Sn-5p* plays a significant function in CB, while *Cs-6s* and *Cs-5p* orbitals play a minor impact. Other published TDOS and PDOS analysis data fit our findings exactly.

Fig. 7(c) shows the DOS of Mn in its 12% phase; the CB and VB are composed of *Mn-3d*, *Sn-5p*, and *Cl-3p*, *Sn-5s*, and *Sn-5p*, respectively. *Mn-3d* states in that energy range are primarily responsible for the non-zero states over the zero-Fermi level.

As the *Mn* concentration increases from 12% to 25%, the number of states in the *Mn-3d* orbital at the Fermi level doubles, as shown in Figure 7(d). However, the VB and CB components of the 25% *Mn*-doped phase are similar to those in the 12.5% doped phase. Figs. 7(g) and (h) illustrate that both the *V* 12.5% and *V* 25% doped phases show a slight shift of the CB edge towards the Fermi level.

The PDOS for *V* 12.5% reveals that the CB is predominantly composed of *Sn-5p* and *V-3d* orbitals, while the VB is made up of *Sn-5s*, *Sn-5p*, and *Cl-3p* orbitals. Although the PDOS characteristics of the *V* 25% doped phase are comparable to those of the *V* 12.5% phase, the DOSs for V is higher in the *V* 25% doped phase.

The PDOS of the 25% *Cr* doped phase is shown in Fig. 7(a). Here, *Sn-5p* and *Cr-3d* orbitals compose CB, whereas *Cs-5p*, *Sn-5s*, and *Cl-3p* orbitals comprise VB. Band structure diagrams show the maxima of the *Cr* states occur near the zero-Fermi level.

As can be seen in Fig. 7(b), the highest VB for the 25% *Ti*-doped phase consists mainly of *Sn-5s*, *Sn-5p*, and *Cl-3p* orbital states, whereas the lowest CB comprises primarily of *Sn-5p* in addition to *Ti-3d* orbital. Fig. 7(f) depicts the 12.5% *Ti* dilution phase, where the CB predominantly comprises *Sn-5p* in addition to *Ti-3d* while the VB is formed by *Sn-5s*, *Sn-5p*, and *Cl-3p* orbital states. However, the PDOS at the *Ti* 12.5% segment shows fewer *Ti* states close to the Fermi level as the *Ti* doping concentration declines.

The *Cs-6s*, *Cs-6p*, *Sn-5s*, *Sn-5p*, and *Cl-3p* orbitals make up the topmost VB, as shown in Fig. 7(e) for the PDOS of the 25% phase of *Fe*. Combining *Sn-5p* and *Fe-3d* orbitals produces the lowest CB. The fact that *Fe* PDOS has a peak of available states at the zero-Fermi level explains why an IB emerges in the band diagram around the Fermi level.

The *Cu*-doped phases were the final transitional element examined. PDOS of *Cu* 12.5% in Fig. 7 (i) reveals, for the first time in our investigation, that the doped material contributes to maximizing VB, specifically *Cu-3d* in addition to *Cl-3p*, *Sn-5s*, and *Sn-5p* orbitals. *Cs-6p* is observed for CB, which is predominantly *Sn-5p* with little contribution from *Cs-6s*. Due to the lack of accessible states at zero Fermi level, neither dilution of *Cu*-doped phases improved optical characteristics.

Zn dilution of 12.5% and 25% is another *d*-block element that we looked at. Figs. 7(m) and (n) show the PDOS for each of them. For *Zn*'s 12.5% phase, the VB comes mostly from the *Sn-5p* orbital and a little bit from the *Zn-4s* orbital. In the CB region, the PDOS for the 25% *Zn* phase shows that the number of available states for *Zn-4s* is a little bit higher. For both types of dilution, TDOS also confirms that no new IBs near VB or CB were made.

We also looked at two elements in the *p*-block, *In* and *Sb*. Figs. 7(k) and (l) show the PDOS of *In* at 12.5% and 25% dilution levels. When compared to the pure $CsSnCl_3$, the 12.5% doped phase did not change much. Here, CB comprises *Sn-5p*, *Cs-6s*, and *Cs-6p* orbitals, and VB comprises *Sn-5s*, *Sn-5p*, *Cl-3p*, *Cs-6s*, and *Cs-5p* orbitals. At zero energy, it can be seen that a small state in the *In-5s* orbital. At *In* 25% phase, CB and VB were almost the same as they were in the 12.5% phase.

Figs. 7 (o) and (p) represent the PDOS of *Sb* at 12.5% and 25%, respectively. At 12.5% doped phase, VB is composed of *Sn-5s*, *Sn-5p*, *Cl-3p*, *Cs-6s*, and *Cs-6p* orbitals, whereas CB is composed of *Sn-5p*, *Cs-6s*, and *Cs-6p* orbitals. At Fermi energy, minor *Sb* states of the *Sb-5p* orbital can be observed approaching the higher energy of CB. In the *Sb* 25% doped phase, VB and CB are virtually identical to the *Sb* 12.5% doped phase; only the *Sb-5p* orbital states are doubled as the doping concentration is doubled.

The Sn^{2+} cation (B site in ABX_3 formation) occupies a central position within the unit cell of $CsSnCl_3$, surrounded by an octahedral coordination of Cl^- (X anions). According to crystal field theory (CFT), in the octahedral coordination geometry, as shown in Fig. 1, when the *Sn* atom is replaced with a transition metal element of *d* block, the six Cl^- ligands are arranged around the doped

metal ion symmetrically, which leads to a large crystal field splitting energy and a large splitting of the metal ion's *d*-orbitals. This splitting can result in a more significant separation between the occupied and unoccupied *d*-orbitals, affecting the material's electronic properties. Specifically, it can lead to the formation of a lower energy set of *d*-orbitals and a higher energy set of *d*-orbitals, which can be referred to as the t_{2g} and e_g sets, respectively. The t_{2g} orbitals are lower in energy and typically have more electrons than the e_g orbitals.

The electronic band structure (Fig. 6) and PDOS (Fig. 7) data reflect the energy levels and DOSs of the electrons in the material. In materials with a high crystal field splitting energy (CFSE) and a partially filled lower energy set t_{2g}, the partitioning of the *d*-orbitals can contribute to the dissociation into electronic states at the Fermi level. This can result in higher DOSs near the Fermi level for the t_{2g} orbitals compared to the e_g orbitals. This difference in the DOS may influence the material's conductivity and mobility.

Band structure and PDOS analysis of all tested phases showed that transition metals *Ti*, *V*, *Cr*, and *Mn* were the best substituent choices. Because, in an octahedral environment, their *3d* t_{2g}-type states can form the partially filled IB.[13] In this case, the *V*-doped phase exhibited exceptional absorption in the visible spectrum, which was corroborated by its other optical and electronic features. Among all doping materials, only V^{2+} possesses a $3d^3$ outer shell, which could be a viable explanation from a chemical standpoint, which is precisely the amount of electron needed to partially fill the *3d* t_{2g}-type states. Ti^{2+}, Mn^{2+}, and Cr^{2+} have $3d^2$, $3d^3$, and $3d^4$ orbitals in their outer shell, respectively. We also noticed the high absorbance of the *V* 12.5%-doped phase is followed by *V* 25%, *Ti*, 25%, *Mn* 25%, *Cr* 25%, and *Mn* 12.5% phases. This further strengthens these correlations. Another aspect to reflect on is the comparative DOSs among them, shown in Fig. 7(r). Recombination, a phenomenon where electrons in the conduction band are captured by the intermediate states and then recombined with holes in the VB, can occur if the DOSs of the intermediate states are too high, which can lower the carrier lifetime and efficiency of the material. In this instance, the *V* 12.5% phase displayed a comparatively low DOS over the zero-Fermi zone, slightly higher than *Mn* 12.5% dilution and lower than all other phases. All of these characteristics point *V* 12.5% phase to be a magnificent $CsSnCl_3$ doped phase for excellent optoelectronics applications.

Although *Zn* is a *d*-block element, it is not a transition element due to the Zn^{2+} filled *d* orbital. As a result, no IB has been seen for the *Zn*-doped phase. The Cu^{2+} also has nine electrons in its *3d* orbital, and the observations represent its contribution to the VB maximum rather than the CB maximum, unlike the other transition elements that we doped. Two *p*-block elements, *Sb* and *In*, exhibited neither IB nor any significant optical or electrical properties based on the criteria examined to date.

As a result of analyzing all of the doped phases in terms of their electronic band structure, PDOS, TDOS, and optical properties, it is evident that only the *V* 12.5%, *V* 25%, *Ti* 25%, *Cr* 25%, *Mn* 12.5%, and *Mn* 25% diluted phases possess the expected optical and electronic properties.

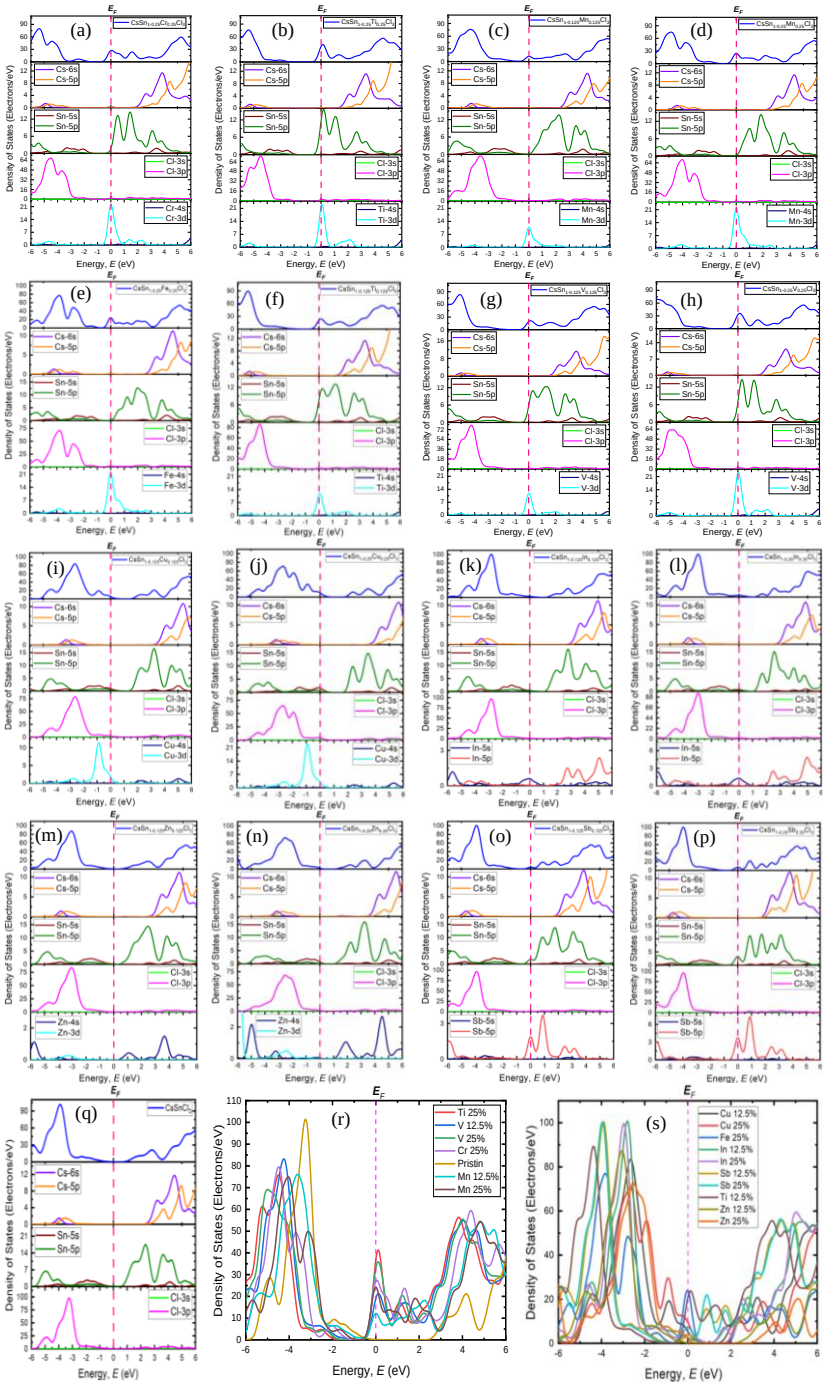

Fig. 7. The PDOS and TDOS for undoped and various cation-doped $CsSnCl_3$ perovskite phases.

7. CONCLUSIONS

This research provides an in-depth examination of various cation-doped $CsSnCl_3$ perovskite phases to identify the best compositions for advanced optoelectronic applications. Seven *d*-block elements, including *Ti*, *V*, *Cr*, *Mn*, *Fe*, *Cu*, and *Zn*, as well as two *p*-block elements, *Sb* and *In*, were studied as dopants at concentrations of 12.5% and 25%. From the detailed analysis, it can be seen that each transition element introduced an IB to the VB and CB of $CsSnCl_3$, hence enhancing its optoelectronic capabilities. Complete investigation and cross-confirmation of the optical and electrical properties of the doped phases led to a greater understanding of their composition. In the optoelectronics study, the *V* 12.5% diluted phase demonstrated the most promising properties. This comprehensive investigation provides detailed insight into the potential of doped $CsSnCl_3$ perovskite for high-quality optoelectronics. The formation of an IB by doping with transition elements offers intriguing options for modifying the material's electrical characteristics and improving its optoelectronic performance. The optical and electrical properties enhance the comprehension of the doped phases and prove their potential for application. Among the investigated doped phases, the *V* 12.5% diluted phase has excellent optoelectronic performance, underscoring the significance of doping concentration management. These results contribute to the fundamental comprehension of doped $CsSnCl_3$ perovskite and pave the way for future advances in the design and manufacture of efficient optoelectronic devices.

ACKNOWLEDGMENTS

The authors are grateful to Bangladesh University of Engineering and Technology (BUET) for the basic research grant for this work, Grant No. Re-6714(6), Dated 06/03/2024.

REFERENCES

[1] Zhang, W., Eperon, G. E. & Snaith, H. J. Metal halide perovskites for energy applications. *Nature Energy* **1**, Article No. 16048 (2016).

[2] Tomšič, Š., Jošt, M., Brecl, K., Topič, M. & Lipovšek, B. Energy Yield Modeling for Optimization and Analysis of Perovskite-Silicon Tandem Solar Cells Under Realistic Outdoor Conditions. *Adv. Theory Simul.* **6**, Article No. 2200931 (2023).

[3] Sheng, R. *et al.* Methylammonium Lead Bromide Perovskite-Based Solar Cells by Vapor-Assisted Deposition. *J. Phys. Chem. C* **119**, 3545–3549 (2015).

[4] Kumar Paul, D. & Akther Hossain, A. K. M. A comprehensive DFT + U investigation of electrical, optical, and structural properties of doped CsSnCl3 Perovskite: Unveiling optoelectronic potential. *Comput. Mater. Sci.* **231**, (2024).

[5] Yin, W. J., Shi, T. & Yan, Y. Unique properties of halide perovskites as possible origins of the superior solar cell performance. *Adv. Mater.* **26**, 4653–4658 (2014).

[6] Shockley, W. & Queisser, H. J. Detailed balance limit of efficiency of p-n junction solar cells. *J. Appl. Phys.* **32**, 510–519 (1961).

[7] Kulbak, M. *et al.* Cesium Enhances Long-Term Stability of Lead Bromide Perovskite-Based Solar Cells. *J. Phys. Chem. Lett.* **7**, 167–172 (2016).

[8] Amraoui, S., Feraoun, A. & Kerouad, M. Performance analysis of lead-free halide double perovskite-based photovoltaic devices for solar cell conception. *J. Alloys. Compd.* **925**, 166509 (2022).

[9] Babayigit, A., Ethirajan, A., Muller, M. & Conings, B. Toxicity of organometal halide perovskite solar cells. *Nature Mater.* vol. 15 247–251 Preprint at https://doi.org/10.1038/nmat4572 (2016).

[10] Ali, Md. S., Das, S., Abed, Y. F. & Basith, M. A. Lead-free CsSnCl3 perovskite nanocrystals: rapid synthesis, experimental characterization and DFT simulations. *Phys. Chem. Chem. Phys.* **23**, 22184–22198 (2021).

[11] Wu, Z. *et al.* Stabilizing the CsSnCl3 Perovskite Lattice by B-Site Substitution for Enhanced Light Emission. *Chem. of Mater.* **31**, 4999–5004 (2019).
[12] Islam, J. & Hossain, A. K. M. A. Narrowing band gap and enhanced visible-light absorption of metal-doped non-toxic CsSnCl3 metal halides for potential optoelectronic applications. *RSC Adv.* **10**, 7817–7827 (2020).
[13] Aguilera, I., Palacios, P., Sánchez, K. & Wahnón, P. Theoretical optoelectronic analysis of MgIn2 S4 and CdIn2 S4 thiospinels: Effect of transition-metal substitution in intermediate-band formation. *Phys. Rev. B Cond. Matter. Mater. Phys.* **81**, (2010).
[14] Datas, A. *et al.* Intermediate band solar cell with extreme broadband spectrum quantum efficiency. *Phys. Rev. Lett.* **114**, (2015).
[15] Luque, A. & Martí, A. Increasing the Efficiency of Ideal Solar Cells by Photon Induced Transitions at Intermediate Levels. *Phys. Rev. Lett.* **78**, 5014–5017 (1997).
[16] Segall, M. D. *et al.* First-principles simulation: ideas, illustrations and the CASTEP code. *J. Phys.: Cond. Matter* **14**, 2717–2744 (2002).
[17] Kohn, W. & Sham, L. J. Self-Consistent Equations Including Exchange and Correlation Effects. *Phys. Rev.* **140**, A1133–A1138 (1965).
[18] Hohenberg, P. & Kohn, W. Inhomogeneous Electron Gas. *Phys. Rev.* **136**, B864–B871 (1964).
[19] Perdew, J. P., Burke, K. & Ernzerhof, M. Generalized Gradient Approximation Made Simple. *Phys. Rev. Lett.* **77**, 3865–3868 (1996).
[20] fischer1992.
[21] Monkhorst, H. J. & Pack, J. D. Special points for Brillouin-zone integrations. *Phys. Rev. B* **13**, 5188–5192 (1976).
[22] Roknuzzaman, M., Ostrikov, K. K., Wang, H., Du, A. & Tesfamichael, T. Towards lead-free perovskite photovoltaics and optoelectronics by ab-initio simulations. *Sci. Rep.* **7**, (2017).
[23] Hoefler, S. F., Trimmel, G. & Rath, T. Progress on lead-free metal halide perovskites for photovoltaic applications: A review. *Monatshefte fur Chemie* **148**, 795–826 (2017).
[24] Jellicoe, T. C. *et al.* Synthesis and Optical Properties of Lead-Free Cesium Tin Halide Perovskite Nanocrystals. *J. Am. Chem. Soc.* **138**, 2941–2944 (2016).
[25] Shannon, R. D. Revised Effective Ionic Radii and Systematic Studies of Interatomie Distances in Halides and Chaleogenides. *Acta Cryst.* **A32**, 751–767 (1976).
[26] Islam, J. & Hossain, A. K. M. A. Narrowing band gap and enhanced visible-light absorption of metal-doped non-toxic $CsSnCl_3$ metal halides for potential optoelectronic applications. *RSC Adv.* **10**, 7817–7827 (2020).
[27] Borriello, I., Cantele, G. & Ninno, D. *Ab initio* investigation of hybrid organic-inorganic perovskites based on tin halides. *Phys. Rev. B* **77**, 235214 (2008).
[28] Barrett, J., Bird, S. R. A., Donaldson, J. D. & Silver, J. The Mössbauer effect in tin(II) compounds. Part XI. The spectra of cubic trihalogenostannates(II). *J. Chem. Soc. A: Inorg. Phys. Th. Chem.* 3105–3108 (1971).
[29] Islam, J. & Hossain, A. K. M. A. Semiconducting to metallic transition with outstanding optoelectronic properties of CsSnCl3 perovskite under pressure. *Sci. Rep.* **10**, (2020).
[30] Kholil, M. I., Bhuiyan, M. T. H., Rahman, M. A., Ali, M. S. & Aftabuzzaman, M. Effects of Fe doping on the visible light absorption and bandgap tuning of lead-free ($CsSnCl_3$) and lead halide ($CsPbCl_3$) perovskites for optoelectronic applications. *AIP Adv.* **11**, (2021).
[31] Peedikakkandy, L. & Bhargava, P. Composition dependent optical, structural and photoluminescence characteristics of cesium tin halide perovskites. *RSC Adv.* **6**, 19857–19860 (2016).
[32] Becke, A. D. A new mixing of Hartree-Fock and local density-functional theories. *J. Chem. Phys.* **98**, 1372–1377 (1993).
[33] Singh, A. K., Janotti, A., Scheffler, M. & Van de Walle, C. G. Sources of Electrical Conductivity in SnO_2. *Phys. Rev. Lett.* **101**, 055502 (2008).